Investigation of TiB distribution characteristics on the microstructure of in situ TiB/Ti6Al4V-ELI manufactured by laser metal deposition

Paul Lekoadi[1*], *Monnamme* Tlotleng[1,2], *Charles* Siyasiya[3] and *Bathusile* Masina[1,2]

[1]CSIR Photonics Centre, Manufacturing Cluster, P O Box 395, Pretoria 0001, South Africa
[2]University of Johannesburg, Mechanical Engineering Science Department, Johannesburg 2012, South Africa
[3]University of Pretoria, Material Science and Metallurgical Engineering Department, Pretoria, South Africa

- **Abstract.** This study presents the investigation of TiB distribution characteristics on the microstructure of in-situ synthesized TiB/Ti6Al4V single-track composites manufacture with laser metal deposition. Ti6Al4V alloy was reinforced by adding TiB_2 ceramic at mass volumes of 0%, 1% and 2% for microstructure modification and mechanical properties enhancement. The TiB/Ti6Al4V composite was characterized using optical microscope (OM), scanning electron microscope (SEM), electron backscatter diffraction (EBSD) and microhardness. It was found that the addition of TiB_2 resulted in the transformation of the prior β-grain into two types of morphologies of dendritic and columnar microstructures. Furthermore, the increase in the amount of TiB_2 resulted in the reduction of the volume fraction of β-Ti phase, with the in situ formed TiB replacing and occupying the β-Ti positions. Deposition at 2% promoted the formation of unmelted TiB2 particles which promoted hardness increase to 496 ± 17 HV.

1 Introduction

Ti6Al4V (also known as Ti64) is recognized and regarded most successful amongst other titanium alloys in various industries which include aerospace, automotive, biomedical and others [1,2]. Its success is attributed to high strength-weight ratio, excellent corrosion resistance and good fracture and fatigue resistance properties [3,4]. However, due to the low service temperature of 480°C, Ti6Al4V components are limited to low and medium temperature applications due to the deterioration of mechanical properties at high temperatures [5,6], which is a major setback. To further improve the high temperature mechanical properties of Ti6Al4V, their matrix is reinforced with hard ceramic materials to manufacture discontinuously reinforced titanium matrix composites (DRTMCs) with a network distribution of reinforcing material.

* PLekoadi@csir.co.za

There are various types of ceramics that have been explored as reinforcing materials such as titanium boride (TiB), titanium diboride (TiB_2), titanium carbide (TiC), silicon carbide (SiC), titanium nitride (TiN), boron carbide (B_4C), graphene nanoplatelets (GNPs) and carbon nanotubes (CNTs) [2,7]. Amongst these ceramic materials, in-situ formed TiB and TiC have been identified as most suitable reinforcement due to their excellent chemical compatibility with titanium [8]. Although, conventional manufacturing methods have proven successful in the manufacturing DRTMCs, there are some major setbacks which include agglomeration of the reinforcement particles, high energy consumption, long processing times and need for post processing [9,10]. These challenges make the using of conventional methods both technologically difficult and economically expensive.

As an alternative, laser additive manufacturing (LAM) is considered as a manufacturing technology which is not only technologically advantageous but also economically competitive to manufacture DRTMCs and other high-performing materials. The manufacturing of DRTMCs with LAM offers an array of many exciting advantages over conventional methods which include production of near-net structural components, high level of flexibility, manufacturing of complex geometries and material and time savings [11,12,13]. Laser metal deposition (LMD) is a type of directed energy deposition (DED) LAM technique that is based on coaxial powder delivery, that can manufacture near-net high-performance components directly from computer aided design (CAD) by simultaneously adding metallic powders, layer upon layer, [14,15]. As such, the manufacturing of TMCs with LAM techniques offers the fabrication of components with unique combination of properties that can benefit high temperature applications. Hence LAM of DRTMCs has attracted interest in various fields, specifically in the aerospace industry.

Most recently, several studies have focused on investigating the microstructure and mechanical properties of TMCs manufactured with LAM. For example, Zhang et al. [7] investigated the microstructure and mechanical properties of TiBw/Ti6Al4V composite manufactured with direct laser deposition (DLD). It was reported that the microstructure of the TiBw/Ti6Al4V composite exhibited dendritic and equiaxed nano-sized TiB networks, with reticular TiBw forming around primary β-Ti in a fine Ti6Al4V matrix. The TiBw/Ti6Al4V exhibited a good combination of strength and plasticity, with ultimate compressive strength and maximum strain values of 1574 MPa and 19.3%, respectively, which was attributed to grain refinement and load transfer effect offered by reticular nano-TiBw. In a different study, Pan et al. [16] reported an enhanced strength of 1121 MPa and ductility of 8.9% on a TiBw/Ti6Al4V composite manufactured with electron beam melting (EBM). The strength enhancement was attributed to both refinement and load bearing refinements afforded by nano sized TiBw together with quasi-continuous reticulated microstructure.

Verma et al. [17] investigated the addition of boron on the microstructure, hardness, and wear performance of TiB/Ti6Al4V composite manufactured with selective laser melting (SLM). The microstructure characterization revealed the formation of randomly distributed colonies of nano/micro TiB particles with needle-like morphology when the volume of boron was 0.1 wt%. The colonies of the nano sized TiB whiskers changed to form connected network morphology when the boron volume was increased to 1 wt%. The hardness was reported to increase linearly with boron addition due to in situ formation of nano sized TiB whiskers, while the wear properties were significantly improved. Fereiduni et al. [18] reported on the creep performance of TiB/Ti6Al4V composite fabricated by SLM. Microstructure characterization showed void formation at the prior β grain boundaries, which were more prevalent at the boundaries perpendicular to the load direction, leading to preferential crack nucleation and propagation sites during loading and promoting intergranular fracture mode. Using laser engineered net shaping (LENS), Nartu et al. [9] evaluated the microstructure of Ti/B_4C composite. The microstructure of the Ti/B_4C

composite was predominantly characterized by in-situ synthesized TiB and TiC precipitates in α-Ti matrix, together with un-melted B_4C and TiB_2 particles. The composite was characterized by a good combination of hardness and wear properties, attributed to the presence of TiB and TiC precipitates.

Using DED, Traxel et al. [19] investigated the high temperature oxidation resistance of Ti/B4C/BN composite. It was reported that the energy density can be varied to achieve composite with excellent oxidation resistance and microstructural stability. Niu et al. [20] manufactured Ti/2Fe-0.1B composite using both LMD and casting and compared their resulting microstructure and mechanical properties. It was reported that both LMD and casting methods produced a microstructure with β-Ti, α-Ti and TiB phases, that co-existed on the Ti/2Fe-0.1B composite, with casting giving a high amount of 5.22% β-Ti compared to 0.13% of LMD. Furthermore, both LMD and casting gave different morphologies of the TiB precipitates, with LMD showing 3D quasi-network TiB structure that formed on the grain boundaries, whereas casting method resulted in TiB needles that were randomly distributed as colonies within larger sized prior β grain boundaries. The LMD Ti/2Fe-0.1B composite gave an ultimate tensile strength (UTS) of 779 MPa, compared to 458 MPa of casting method, which was attributed to synergy of grain size strengthening and grain boundary strengthening effects.

Finally, Fang et al. (2021) investigated the microstructure evolution and the role of nano TiB on TiB/Ti composite fabricated with DLD. It was found that the TiB/Ti composite formed a three-dimensional (3D) in situ ultrafine network structure consisting of nano TiBw whiskers with dendritic and equiaxed morphology. The two morphologies were attributed to boron induced constitutional supercooling and subsequent nucleation and growth of the primary β-Ti. A good combination of 636 MPa strength and 10.6% elongation was achieved on the TiB/Ti composite, which was attributed to the unique configuration of the TiB network and Hall-Petch strengthening. The reviewed studies show that the manufacturing of TMCs with different LAM techniques lead to different microstructural characteristics that are obviously characterized by different mechanical properties. However, literature on the manufacturing of TiB/Ti6Al4V composite manufactured with LMD for high temperature investigations is lacking. This implies that the microstructure of LMD TiB/Ti6Al4V composite still needs to be investigated. Therefore, this study focused on investigating the distribution characteristic of TiB on the microstructure and hardness properties of TiB/Ti6Al4V composite manufactures with LMD.

2 Experimental Procedure

2.1 Materials

A spherical grade 23, pre-alloyed Ti6Al4V- extra low interstitial (ELI) with particle size distribution in the range 45 - 100 μm (supplied by TLS Technik GMbH & Co, Bitterfeld, Germany) and TiB_2 powder with particles size in the range 50-100 μm (supplied by Stanford Advance Material) were deposited on a Ti6Al4V substrate with dimensions 100 mm x 100 mm x 6 mm. The base plate was subjected to sandblasting to prepare it for deposition. The morphology of the Ti6Al4V-ELI and TiB_2 powders together with their corresponding particle size distribution (PSD) curves are presented in Figure 1. PSD measurements were conducted using the Microtrac Total Solution Particle Characterization Instrument.

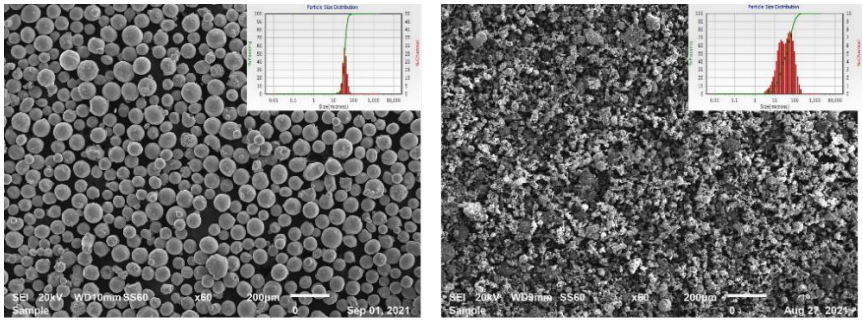

Fig. 1. Powder morphology of (a) Ti6Al4V-ELI, and (b) TiB_2 powders.

Figure 1(a) shows that Ti6Al4V-ELI particles were highly spherical and smooth, with PSD in the range 26-54 µm. In contrast, a mixture of spherical and irregular shaped particles was observed on the TiB_2 powder, with PSD in the range 11-120 µm as shown in Figure 1(b).

2.2 Methods

A LMD system coupled with an IPG fibre laser of wavelength 1073 nm and integrated with a KUKA robot and 3-way nozzles was used to deposit the samples. A GTV powder system (D-57629), equipped with two powder feed hoppers was used was used to deliver the Ti6Al4V-ELI and TiB_2 powders through the carrier gas during deposition. The Ti6Al4V-ELI was deposited at a constant mass deposition rate, while the TiB_2 powder was deposited at varying mass deposition rates of 0%, 1% and 2%, respectively. Single-track samples of approximately 40 mm were deposited using optimized process parameters. Argon gas was used as a protective gas, at gas flow rate of 15 l/min to prevent the samples from contamination with oxygen.

2.3 Metallographic preparation and characterization

The sample were metallographically prepared according to metallurgical standard [21] and etched were etched with Kroll's reagent, a solution containing 100ml H_2O, 1-3mL HF and 2-6mL HNO_3. The metallographically prepared and etched samples were observed for microstructure using an Olympus BX51M Optical Microscope (OM) and Joel JSM-6010PLUS/LA scanning electron microscope (SEM). A Zeiss Cross Beam 540 FIB-SEM electron backscatter diffraction (EBSD) machine with Oxford Atlas software was used for pattern acquisition and analysis of the grain size maps, crystal structures and phases present in the composite. It must be noted that the EBSD analysis was conducted on a polished but unetched surface. Hardness measurements were performed using Matsuzawa Seiko Vickers model MHT-1 micro-hardness machine. All measurements were done using a diamond tip indenter while applying a force of 0.3 kgf and dwell time of 10 seconds. For all samples, three hardness patterns were measured, and the average was calculated as the hardness of the material.

3 Results and Discussions

3.1 Microstructure

The overview optical microstructures single-track Ti6Al4V and TiB/Ti6Al4V composite samples are presented in Figure 2.

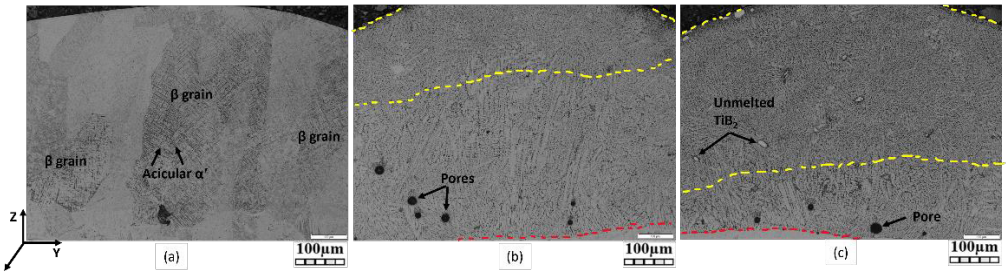

Fig. 2. OM images of the samples, (a, b) Ti6Al4V-ELI, (b) 1% TiB_2, and (c) 2% TiB_2.

The microstructure of the Ti6Al4V-ELI sample was characterized by long columnar prior β grains that were elongated parallel to the built direction (z-axis) as can be seen in Figure 2(a). According to literature, the growth of the columnar prior β-grain follows an overall downward heat flow direction, whose preferred direction is <100> which is preferred by the body centred cubic (bcc) lattice structure [22,23]. In addition, a sharp acicular martensite α′ phase was present inside these columnar β grains and were embedded as laths as shown in Figure 2(a). The formation of the acicular martensite α′ phase was attributed to high cooling rates associated with the LMD process [14]. Since Ti6Al4V-ELI is a dual phase (α+β) alloy, the formation of the martensite α′ phase followed a diffusionless transformation from fully β-phase (β→α′) due to high cooling rates that can reach up to 13000 K/s [24,25] during DED processing. The martensite α′ phase is known to promote strength increase, but at the cost of elongation (ductility) [26]. Similar type of martensitic α′ microstructure on Ti6Al4V alloy manufactured with DED were reported in literature [25,27,28].

The addition of 1% TiB_2 to the Ti6Al4V matrix initiated a major microstructural change, with complete transformation of the columnar β-grains and the martensite α′ phase as can be seen in Figure 2(b). It was obvious that the columnar grains were transformed into dendritic and columnar morphologies, resulting in dendrites dominated region (yellow colour section) and columnar grains dominated region (red colour section) as shown in Figure 2(b). To identify these two regions on the single-track sample, the columnar grains dominated region formed at the bottom of the sample (closer to the substrate) whereas the dendrites dominated region formed at the top of the sample (away from the substrate towards the edge). The difference in morphologies was attributed to the difference in heat loss experienced by the sample in the two regions during cooling, with the top region experiencing fast cooling (or supercooling), while the bottom part experienced slow cooling [17]. It must be noted that the columnar grains dominated region formed part of the heat affected zone (HAZ), hence the formation of columnar grains [14]. According to Xue et al. (2019), boron is one of the most effective elements for forming constitutional supercooling zone which plays an important role columnar transition of primary β-Ti.

While the martensite α′ phase was also not visible after the addition of 1% TiB_2, the microstructure was dominated by in-situ formed TiB phase. It is well known that boron promotes grain refinement and can also inhibit the formation of martensite α′ phase is some cases [7,17]. Therefore, the addition of 1% TiB_2 transformed the parent columnar β-grain and inhibited the formation of the martensite α′ phase. The grain structure and morphology will be discussed next.

Deposition of TiB_2 at 2% increased the number of dendrites, resulting in an increase in the area of the dendrites dominated region as can be seen in Figure 2(c). In other words, the higher amount of TiB_2 promoted the formation of dendritic structure, which resulted in an obvious pushing of the columnar grains dominated region closer to the substrate and forming a smaller area of the columnar grains dominated region. This observation was attributed to the increase in the amount of TiB_2 present. Furthermore, 2% mass volume promoted the formation of unmelted TiB_2 particles as shown in Figure 2(c). The presence of unmelted TiB_2 particles was attributed to insufficient energy density to fully melt the TiB_2 particles during the LMD process [23,30]. To further examine the microstructure of the samples at higher magnification, together with size, shape, distribution, and orientation of the TiB phases and matrix, EBSD phase distribution maps together with their corresponding scanned micrographs, and the measured phase volume fractions of the Ti6Al4V-ELI and TiB/Ti6Al4V-ELI composites are presented in Figure 3 and Table 1, respectively. It is important to note that the red and blue parts represent hexagonal and cubic titanium, while the yellow and green parts represent TiB and TiB_2 respectively. The black part represents regions that were not recognized by the EBSD during scanning of the samples.

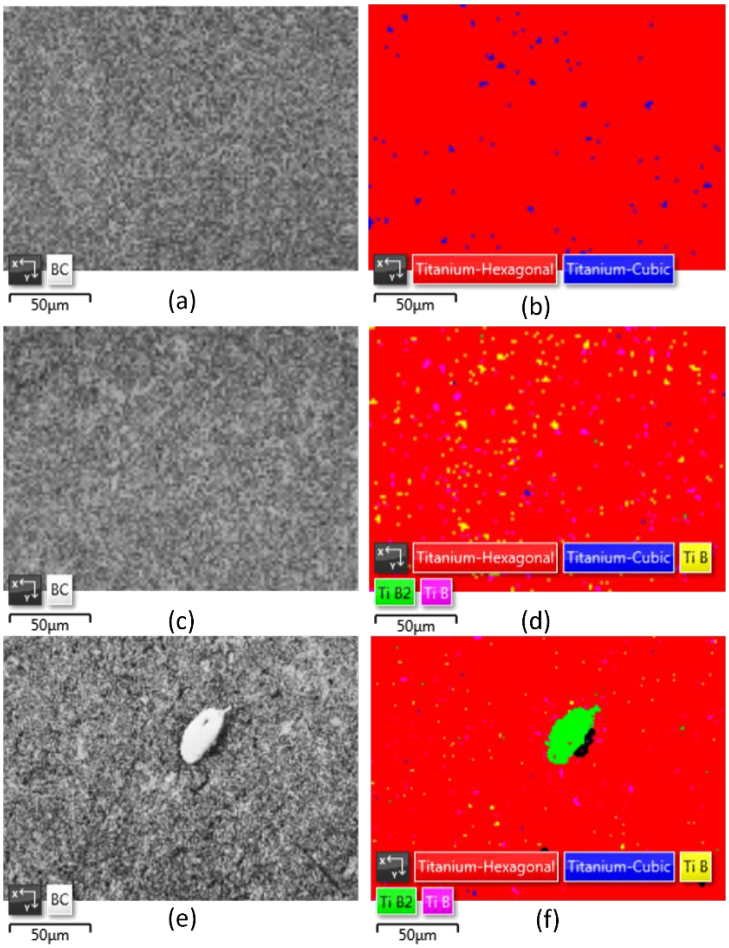

Fig. 3. SEM micrographs and EBSD phase distribution maps of the samples, (a, b) Ti6Al4V-ELI, (c, d) 1% TiB_2, and 2% TiB_2.

Table 1 : Phase volume fractions of the samples.

	Volume fraction (%)		
Phase	**Ti6Al4V**	**1% TiB_2**	**2% TiB_2**
α′-Ti	98.93	95.47	96.59
β-Ti	1.07	0.77	0.05
TiB	0	4.44	1.1
TiB_2	0	0.33	1.88

The EBSD phase distribution map of Ti6Al4V-ELI in Figure 3(b) showed the presence of two phases, namely, hexagonal-Ti 9 (hcp) and cubic-Ti (bcc) which were identified as martensite α′ (or α) and β-Ti phases. Since martensite α′ and α phase have the same hcp crystal structure, the hcp on the Ti6Al4V sample (Figure 3b) was interpreted as martensite α′ based on the OM observations. The measured volume fraction of martensite α′ phase (hcp) was 98.93% and 1.07% for β phase (bcc) in the Ti6Al4V-ELI alloy, without the presence of TiB or TiB_2 phases as can be seen in Table 1.

From Figure 3(d), the 1% sample presented the presence of four phases, namely, α-Ti, β-Ti, TiB and TiB_2. While the presence of TiB_2 was due to insufficient energy density, the appearance of TiB phase suggested an in-situ reaction between the molten Ti6Al4V-ELI and TiB_2 has occurred. The presence of TiB after LAM was reported in other studies [1, 31]. To explain the formation of TiB during the LMD process, a binary Ti–B phase diagram is presented in Figure 4.

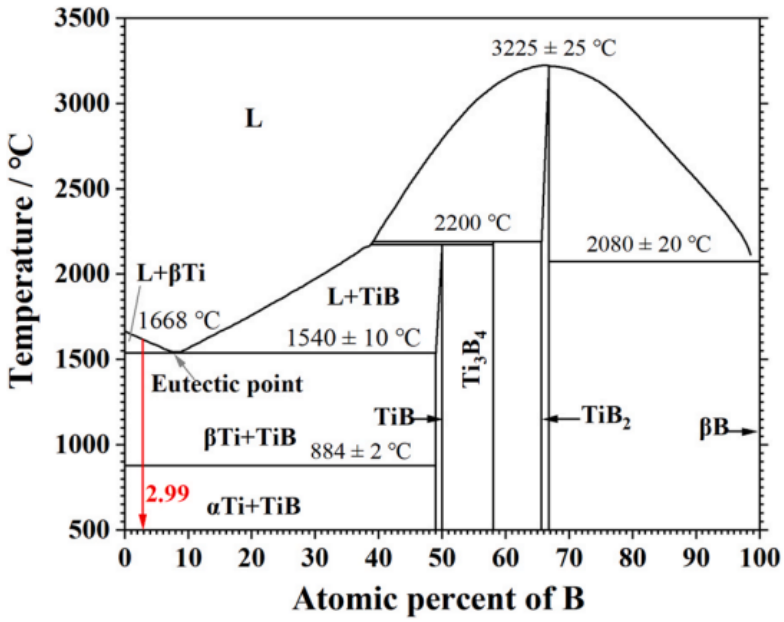

Fig. 4. Binary Ti – B phase diagram [1].

During LMD process, both the Ti6Al4V-ELI and TiB_2 are melted due to the high energy laser beam [1], and therefore according the TiB phase diagram (Figure 3), the following chemical reactions are possible in the binary system [7]:

$$Ti + TiB_2 \rightarrow 2TiB \quad (\Delta G = -10\ kcal/mol) \quad (1)$$
$$Ti + 2B \rightarrow TiB_2 \quad (\Delta G = -60\ kcal/mol) \quad (2)$$
$$Ti + B \rightarrow TiB \quad (\Delta G = -40\ kcal/mol) \quad (3)$$

The negative values of the Gibbs free energy (ΔG) in equation 1, 2 and 3 indicates a spontaneous formation of TiB and TiB_2. It is important to note that the solidification paths vary based on the boron content in the molten liquid with a decrease in temperature or during cooling (Figure 4). When the boron content is higher than the eutectic point, the solidification path is defined as Liquid (L) → L + primary TiB → primary TiB + Eutectic (TiB + β-Ti) → α-Ti + β-Ti + TiB. Due to the high cooling rates associated with the LMD process, the eutectic β-Ti transform into martensite α′ upon cooling, hence the in situ formed TiB is dispersed in a martensitic α′ matrix. Equation 1 and 3 explains the formation of in situ synthesized TiB even though the starting material was TiB_2. The distribution characteristics of the TiB in the Ti6Al4V matrix is clearly seen in Figure 3(d). It can be seen that the TiB phase formed on the grain boundaries of parent prior β-grain.

Formation of the TiB phase on the grain boundaries was attributed to surface tension formed by steep thermal gradients between the centre edge of the molten pool and nucleation of the β-Ti caused by high laser energy radiation [32]. The distribution of TiB on the β-grain boundaries is known to enhance strength and elongation at higher temperatures [33,34,35]. Also, the existence of TiB is known to improve the strength and hardness of the materials [1,14]. Table 1 shows that 1% sample measured volume fractions of 95.47%, 0.77%, 4.44% and 0.03% for the martensite α′-Ti, β-Ti, TiB and TiB_2, respectively. This implies the volume fraction of both martensite α′ and β-phase decreased after the addition of 1% TiB_2, which is also clearly demonstrated by EBSD phase distribution map in Figure 3(d). Furthermore, the presence of TiB phase confirms the occurrence of reactions 1 and 3.

While deposition of TiB_2 at 2% also presented martensite α′, β, TiB and TiB_2 phases, the presence of bigger sized TiB_2 particles which increased the volume fraction of TiB_2 to 1.88% was observed. Furthermore, the volume fraction martensite α′ was also increased, while the volume fraction of β-Ti and TiB were decreased 0.05% and 1.1% respectively (Table 1). This implies that increasing the volume fraction promotes the formation of unmelted particles while reducing the amount of β-Ti phase. According to Zhang et al. [7], when the boron content is higher, more energy is needed to melt the powders, consequently leading to unmelted particles and poor interface fusion. Meanwhile, the size of the TiB particles in Figure 3(f) were significantly reduced, while bigger unmelted TiB_2 particles were observed. The presence of TiB_2 phase support the observation that was made on the OM analysis where unmelted TiB2 particles were observed.

3.2 Hardness

It is well known that that the dispersion characteristics of the in situ formed TiB will have an influence on the mechanical properties of the TMC. The graphs showing hardness profiles and average hardness values of the Ti6Al4V-ELI and TiB/Ti6Al4V-ELI composite are shown in Figure 5 and Table 2 respectively.

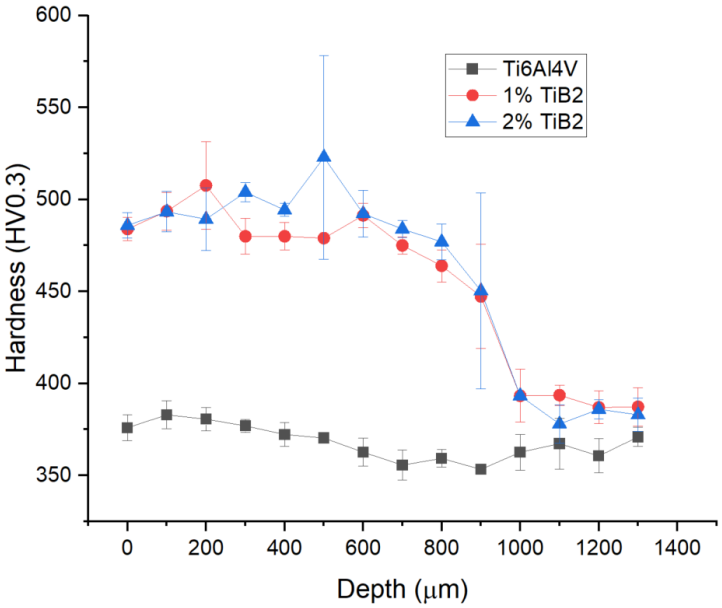

Fig. 5. Hardness profiles of the samples.

Table 2. Average hardness of the samples.

Sample	Hardness ($HV_{0.3}$)
Ti6Al4V	368 ± 7
1%	488 ± 9
2%	496 ± 17

Figure 5 and Table 2 hardness shows that the Ti6Al4V-ELI gave the lowest hardness of 368 ± 7 HV, which was associated with the martensitic α′ microstructure. Furthemore the Ti6Al4V sample gave a stable hardness profile compared to the TiB/Ti6Al4V-ELI composites. The hardness was increased to 488 ± 9 when 1% TiB_2 was added to the Ti6Al4V alloy, attributed to the formation of TiB whiskers (Figure 3c). A further hardness increases to 496 ± 17 HV was recorded for the 2% sample, which was attributed to the presence of both TiB and unmelted TiB2 particles. This implies that the hardness increased with increasing mass deposition volume.

4 Conclusion

In this work, single-track Ti6Al4V-ELI and TiB/Ti6Al4V-ELI composites were manufactured with LMD to understand the distribution characteristics of TiB on microstructure and hardness properties for their application in high temperature environments. The following conclusions have been drawn:

- The addition of TiB_2 into Ti6Al4V-ELI promotes the formation of two different morphologies on the sample, with columnar grain dominated regions forming closer to the substrate and dendrites dominated region forming away from the substrate due to difference in cooling rate.

- Addition of 1% TiB_2 favour the columnar distribution morphology of TiB whereas 2% favours the formation of dendritic distribution morphology, with hardness increasing with the deposition volume.
- Deposition of TiB_2 at 2% is ideal for achieving cosnsitent distribution of TiB in the TiB/Ti6Al4V composite.

References

1. E. Fereiduni, A. Ghasemi, M. Elbestawi, J. Alloys Compd. **896**, (2022)
2. P.M. Lekoadi, M. Tlotleng, B.N. Masina, Suid-Afrikaanse Tydskrif vir Natuurwetenskap en Tegnologie, **40**, (2021)
3. L.Y. Qin, J.H. Men, L.S. Zhang, S. Zhao, C.F. Li, G. Yang, W. Wang, Mater. Sci. Eng. **759** (2019)
4. Z.W. Yan, L.Q. Fu, S.L. Wang, Y. Wang, Z.Q. Ma, D.P. Wang, Addit. Manuf. **39**, (2021)
5. L. Huang, Q. An, L. Geng, S. Wang, S. Jiang, X. Cui, R. Zhang, F. Sun, Y. Jiao, C. Wang, Adv. Mater. **33**, (2021)
6. Q. An, L. Huang, Q. Qian, Y. Jiang, S. Wang, R. Zhang, L. Geng, J. Mater. Sci. Technol. **119**, (2022)
7. Q. Zhang, W. Sun, S. Xu, X. Zhang, J. Wang, C. Si, J. Alloys Compd. **922**, (2022)
8. K. Morsi, V.V. Patel, J. Mater. Sci. **42**, (2007)
9. M.S.K. Nartu, M. Pole, S.A. Mantri, R.S. Haridas, T.W. Scharf, B. McWilliams, K. Cho, S. Mukherjee, N.B Dahotre, Addit. Manuf. **46**, (2021)
10. H. Attar, S. Heghihi, D. Kent, X. Wu, M.S. Dergusch, Mater. Sci. Eng. 3, (2018)
11. M. Fang, Y. Han, Z. Shi, G. Huang, J. Song, W. Lu, Compos. **211**, (2021)
12. D. Herzog, V. Seyda, E. Wycisk, C. Emmelman, Acta. Mater. 117, (2016)
13. I. Gibson, D.W. Rosen, B. Stucker, (Addit. Manufac. Technol. (2010)
14. P.M. Lekoadi, M. Tlotleng, C.W. Siyasiya, B.N. Masina, MRS Adv. **388**, (2023)
15. A. Vafadar, F. Guzzomi, A. Rassau, K. Hayward, Appl. Sci. **11**, (2021)
16. D. Pan, S. Li, L. Liu, X. Zhang, B. Li, B. Chen, M. Chu, X. Hou, Z. Sun, J. Umeda, K. Kondoh, Addit. Manuf. **50**, (2022)
17. P.K. Verma, S. Warghane, U. Nichul, P. Kumar, A. Dhole, V. Hiwwarkar, Mater. Charact. **172**, (2021)
18. E. Fereiduni, A. Ghasemi, M. Elbestawi, J. Manuf. Process. **70**, (2021)
19. K.D. Traxel, A. Bandyopadhyay, Mater. Des. **212**, (2021)
20. J. Niu, G. Dai, Y. Guo, Z. Sun, Z. Dan, Y. Dong, H. Chang, I.V. Alexandrov, L. Zhou, Compos. **261**, (2021)
21. P. Lekoadi, M. Tlotleng, K. Annan, N. Maledi, B. Masina, Metals. **255**, (2021)
22. H. Lu, L. Wu, H. Wei, J. Cai, K. Luo, X. Xu, J. Lu, Addit. Manuf. **55**, (2022)
23. P.M. Lekoadi, M. Tlotleng, K.A. Annan, B. *Masina, Effect of heat treatment on the microstructure, hardness and tensile properties of high-speed selective laser melted Ti6Al4V,* In proceedings of the 23rd RAPDASA-RobMech-PRASA-CoSAAMI Conference, 8-11 November 2022, Stellenbosch, South Africa (2022).
24. A. Dass, A. Moridi, Coatings, 418, (2019)

25. M. Hayat, H. Sigh, Z. He, P. Cao, Compos. **121**, (2019)
26. S. A. Shalnova, M.O. Gushchina, D.A. Strekalovskaya, E.L. Alekseeva, O. G.Klimova-Korsmik, J. Alloys Compd**, 899**, (2022)
27. H. A. Hegab, Manuf. Rev. 3, (2016)
28. D. Algius K. I. Kourousis, C. Wallbrink, Metals.**75**, (2018)
29. A. Xue, X. Lin, L. Wang, J. Wang, W. Huang, Mater. Des. **181**, (2019)
30. A.P.I Poopola, L. Phume, S. Pityana, V.S. Aigbodion, Surf. Coat. Technol. **285**, (2016)
31. H. Li, Z. Yang, D. Cai, D. Jia, Y. Zhou, Mater. Des. **185**, (2020)
32. Y. Hu, W. Cong, X. Wang, Y. Li, F. Nind, H. Wang, Compos. Part B. **133**, (2018)
33. M. Fang, Y. Han, Z. Shi, G. Huang, J. Song, Compos. **211**, (2021)
34. L.J. Huang, L. Geng, Y. Fu, B. Kaveendran, H.X. Peng, Corros. Sci. **69**, (2013)
35. Z.W. Yang, L.Q. Fu, S.L. Wang, M. Zhang, Y. Wang, Z.Q. Ma, D.P. Wang, Addit. Manuf. **39**, (2021)